# Average neutron cross sections of $^{99}$Tc

G. Noguere,* B. Geslot, A. Gruel, P. Leconte, and L. Salamon
*CEA, DEN Cadarache, F-13108 Saint Paul Les Durance, France*

J. Heyse, S. Kopecky, C. Paradela, and P. Schillebeeckx
*EC-JRC-IRMM, B-2440 Geel, Belgium*

(Received 11 March 2020; accepted 24 June 2020; published 29 July 2020)

$^{99}$Tc has been the subject of several experimental programs at the JRC-Geel since the late 1990s. This work presents new transmission data measured at the GELINA facility with the time-of-flight technique, whose simultaneous analysis with past transmission experiments provided a revised set of resonance parameters up to 5 keV. An iterative analysis between the resonance and "continuum" energy ranges leads to average resonance parameters [$S_0 = 0.51(3)$, $\langle\Gamma_{\gamma_0}\rangle = 137(7)$ meV, $D_0 = 12.8(2)$ eV] and theoretical average capture cross sections consistent with those reported in the literature. At $E = 30$ keV, we obtain a capture cross section of 1076(45) mb and a Maxwellian-averaged cross section (MACS) of 1016(43) mb. The agreement with the recommended MACS value of 933(47) mb remains within the quoted uncertainties. This result demonstrates the performances of transmission experiments to provide reliable theoretical capture cross sections for long-lived fission products in the energy range of interest for *s*-process nucleosynthesis calculations.

DOI: 10.1103/PhysRevC.102.015807

## I. INTRODUCTION

The modelization of the neutron-induced reactions of long-lived fission products is still an issue due to the lack of accurate reaction data over a broad neutron energy range. Experimental accuracy limitations are closely related to the activity of the samples. The signal-to-noise ratio can be improved by using time-of-flight facilities designed to deliver high instantaneous neutron flux. The present work investigates a different strategy and shows how average neutron capture cross sections in the keV energy range can be predicted by using transmission experiments carried out at the GELINA facility of the JRC-Geel (Belgium).

The study is restricted to intermediate-mass nuclei for which most of the neutron widths $\Gamma_{\lambda,n}$ of the resonances $\lambda$ are smaller that the radiation widths $\Gamma_{\lambda,\gamma}$. $^{99}$Tc is a good candidate for exploring the performances of this theoretical approach because the simultaneous analysis of transmission data measured with thin and thick samples may provide radiation width values for a few numbers of low-energy *s*-wave resonances. Such results are needed to obtain an *s*-wave average radiation width $\langle\Gamma_{\gamma_0}\rangle$ which is used to normalize the $\gamma$-ray transmission coefficients involved in the theoretical description of the average capture cross section.

The isotope of technetium with the longest half-life produced via the *s* process is $^{99}$Tc ($2.1 \times 10^5$ y). Its occurrence makes it a reliable indicator for studying the stellar evolution through the asymptotic giant branch (AGB) phase [1–3]. In parallel, theoretical and experimental works on $^{99}$Tc [4–7] point out large differences between the experimental neutron capture cross sections in the keV neutron energy range, which also corresponds to the energy range of interest for *s*-process nucleosynthesis calculations. Figure 1 shows that similar inconsistencies exist between the JEFF-3.3 [8], ENDF/B-VIII [9], and JENDL-4.0 [10] evaluated neutron cross section libraries. At 30 keV, the $^{99}$Tc$(n,\gamma)$ cross section ranges between 863 mb to 1151 mb.

An extensive experimental program was already undertaken in the late 1990s at the GELINA facility for extracting $^{99}$Tc neutron resonance parameters up to 10 keV. The experimental work is described in Ref. [11] and the resonance analysis was completed by Gunsing *et al.* [12]. Effective radius $R'$, average radiation width $\langle\Gamma_{\gamma_0}\rangle$, mean level-spacing $D_l$, and neutron strength function $S_l$ for orbital angular momenta $l = 0$ (*s*-wave resonances) and $l = 1$ (*p*-wave resonances) were deduced from the neutron resonance analysis of transmission data. The goal of the present study is to provide a set of revised $l$-dependent resonance parameters by adding in the neutron resonance analysis new transmission data recently measured at the GELINA facility. Average neutron cross sections will be derived thanks to mathematical relationships between the model parameters involved in the *R*-matrix [13] and *S*-matrix [14] formalisms, which are respectively used to describe the resonance and "continuum" energy ranges of the neutron cross sections.

The mathematical relationship between the *R*-matrix and *S*-matrix formalisms is explained in the second section. Principles of the resonance analysis and of the optical model calculations are presented in the third and fourth sections. Average neutron resonance parameters and the agreement between the theoretical and experimental neutron cross sections are discussed in the last section.

*gilles.noguere@cea.fr

 

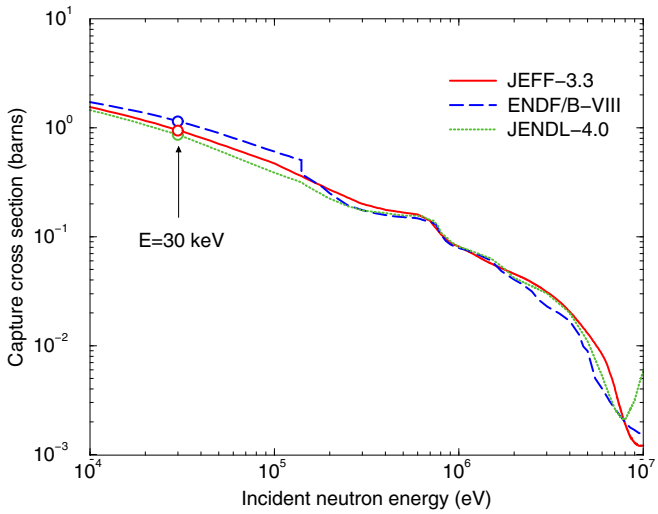


FIG. 1. $^{99}$Tc capture cross section as a function of the incident neutron energy recommended in the JEFF-3.3 [8], ENDF/B-VIII [9], and JENDL-4.0 [10] evaluated neutron cross section libraries.

## II. THEORY OF AVERAGE CROSS SECTION

Experimentally we can observe that there is a continuous transition in the neutron cross sections from the extreme situation of well-isolated resonances to complete overlap. This transition can be described within the $R$-matrix theory by using appropriate approximations. One of the first description of the theory of average cross section was proposed in 1954 by Feshbach *et al.* [15]. This work indicates how the $R$-matrix and $S$-matrix formalisms coexist between the resonances and "continuum" energy ranges. The main ingredients of the theory are exemplified in the case of the capture process. More information and references can be found in Ref. [16].

### A. Radiative capture reaction

Systematic studies on the radiative capture cross sections in the resonance range and beyond are well documented in the literature [17,18]. Average capture cross section calculations are based on the Hauser-Feshbach formula with width fluctuation corrections [19,20]. For an entrance channel $c = \{l, J\}$, mainly defined by the orbital angular momentum of the incoming neutron $l$ and total angular momentum $J$ of the whole neutron-target system, the capture cross section $\sigma_{\gamma_c}$ can be written as

$$\sigma_{\gamma_c} = \frac{\pi}{k^2} g_J \frac{T_{n_c} T_{\gamma_c}}{\sum_\beta T_{\beta_c}} W_{n\gamma_c}, \tag{1}$$

in which $k$ is the wave number of the incoming neutron in the center-of-mass system and $g_J$ is the statistical spin factor:

$$g_J = \frac{2J+1}{(2i+1)(2I+1)} \tag{2}$$

with $i$ and $I$ being the spins of the neutron and target nucleus. For nonfissile nuclei, the neutron and $\gamma$-ray transmission coefficients $T_{n_c}$ and $T_{\gamma_c}$ are the main quantities involved in the statistical model calculations below the energy threshold of the inelastic neutron scattering reaction. At low incident neutron energy, the $\gamma$-ray transmission coefficients are normalized to $T_{\gamma_0}$ which depends on the ratio of the average radiation width $\langle\Gamma_{\gamma_0}\rangle$ to the mean level spacing for $s$-wave resonances having zero orbital angular momentum ($l = 0$):

$$T_{\gamma_0} = 2\pi \frac{\langle\Gamma_{\gamma_0}\rangle}{D_0}. \tag{3}$$

The mathematical expression of the neutron transmission coefficients relies on the wave description of the nuclear scattering through the scattering matrix elements $\mathcal{S}_c$:

$$T_{n_c} = 1 - |\mathcal{S}_c|^2, \tag{4}$$

whose low energy values depend on two quantities, namely the neutron strength function $S_c$ and channel radius $a_c$.

### B. Square-well approximation

Central to the $R$-matrix and $S$-matrix frameworks is the division of the configuration space at an appropriate channel radius $a_c$ chosen to match the solution of the Schrödinger equation with its corresponding asymptotic expression, where the complex mean-field potential vanishes. The size of the internal region is not defined. In this work, this ambiguity is solved by choosing $a_c$ such that the optical model (OM) and its equivalent square-well (SQW) provide the same phase shifts $\phi_l^{OM} = \phi_l^{SQW}$ at the common channel radii. The resonance theory determines the hard-sphere phase shifts $\phi_l^{SQW}$ from the precisely known radial wave functions at the channel radius $a_c$. Denoting $\rho = ka_c$, one obtains

$$\begin{aligned} \phi_0^{SQW}(\rho) &= \rho, \\ \phi_1^{SQW}(\rho) &= \rho - \tan^{-1}(\rho), \\ \phi_2^{SQW}(\rho) &= \rho - \tan^{-1}\left(\tfrac{3\rho}{3-\rho^2}\right). \end{aligned} \tag{5}$$

Equivalent hard-sphere channel radii can then be obtained from the least-squares fit of $\phi_l^{OM}$ with Eq. (5). In that case, the neutron strength function are given by [21]

$$\frac{\pi S_c \sqrt{E} P_l^{SQW}}{2P_0^{SQW}} = \frac{2\left(\beta_c - \theta_c^2\right)}{1 + 2\theta_c^2 - 2\beta_c + (1-2\beta_c)\cos\left[2\phi_c^{SQW}\right] - 2\alpha_c \sin\left[2\phi_c^{SQW}\right]} \tag{6}$$

with $P_l^{SQW}$ being the centrifugal-barrier penetrability

$$\begin{aligned} P_0^{SQW}(\rho) &= \rho, \\ P_1^{SQW}(\rho) &= \tfrac{\rho^3}{1+\rho^2}, \\ P_2^{SQW}(\rho) &= \tfrac{\rho^5}{9+3\rho^2+\rho^4}. \end{aligned} \tag{7}$$

Parameters $\alpha_c$, $\beta_c$, and $\theta_c$ represent the real part, the imaginary part and the absolute value of $C_c$ which is related to the $S$-matrix elements by $\mathcal{S}_c = 1 + 2iC_c$.

### C. Average $s$-wave resonance parameters

The expressions (3), (5), and (6) indicate that the parameters of interest for this work are the average radiation width $\langle\Gamma_{\gamma_0}\rangle$, the mean level spacing $D_0$, the neutron strength function $S_l$, and the channel radius $a_c$. If the latter $l$-dependent radius can be directly derived from optical model calculations, values for the other parameters in the $s$-wave channel can be established from the statistical analysis of the resonance parameters. This approach relies on the statistical nature of the neutron resonances in which nonstatistical effects in both $s$ and $p$ waves are assumed to be negligible.

An unambiguous identification of the $l$ dependence (or parity) of the observed resonances is hardly achievable at the GELINA facility. The $s$-wave resonances $\lambda$ included in the statistical analysis are then selected according to a $l$-assignment method relying on the probability density function of the reduced neutron widths hypothesized by Porter-Thomas [23]. Such an approach was applied to $^{99}$Tc in Refs. [6,12], in which the $l$ assignment is driven by the Bayesian conditional probability that a resonance is a $p$ wave, given its neutron width value. The selection is made according to a probability threshold, namely Bayesian threshold, below which the resonance is assumed to have a zero orbital angular momentum.

In order to avoid as much as possible an arbitrary choice of this Bayesian threshold, $l$ assignment can be done simultaneously with the determination of the $s$-wave neutron strength function $S_0$ and mean level spacing $D_0$ through the cumulative distribution function of the $s$-wave reduced neutron widths. The reduced neutron width $\Gamma_n^0$ is defined as the ratio of the $s$-wave neutron widths to the square root of the resonance energy, whose average value is related to $S_0$ and $D_0$ as follows:

$$\left\langle\Gamma_n^0\right\rangle = S_0 D_0, \tag{8}$$

in which the mean level spacing is simply given by

$$D_0 = \frac{E_{\max} - E_{\min}}{N_0 - 1}. \tag{9}$$

Energies $E_{\min}$ and $E_{\max}$ define the energy limits of the statistical resonances and $N_0$ stands for the number of estimated resonances between $E_{\min}$ and $E_{\max}$. The lower energy limit corresponds to the first $s$-wave resonance energy. The upper energy limit depends on the number of missing resonances. Therefore, $\langle\Gamma_n^0\rangle$ and $N_0$ are free parameters, whose values depend on the choice of $E_{\max}$. In this work, the upper energy limit of the statistical analysis is defined so that the fraction of missing levels remains lower than 5% of the number $N_{\exp}$ of experimentally observed resonances. In the mean time, posterior $S_0$ and $D_0$ values are also monitored thanks to the cumulative distribution of the $s$-wave reduced neutron width and of the number of $s$-wave resonances as a function of the resonance energies. In the statistical hypothesis, the slope of the obtained distributions depends linearly of the neutron strength function and level density ($1/D_0$), respectively.

Once the sequence of $s$-wave resonances is well established, an average radiation width $\langle\Gamma_{\gamma_0}\rangle$ can emerge from the data. In neutron resonance spectroscopy, the average radiation width is often approximated by the mean value of individual radiation widths $\Gamma_{\lambda,\gamma}$, whose values can be obtained from the total width of few low-energy resonances $\lambda$. As a consequence, it is not so unusual to observe in the literature a large spread between average radiation widths for a same compound system. Various experimental uncertainties can be invoked to explain such issues. In the present work, most of them will be propagated through the resonance analysis by Monte Carlo [22]. Other sources of biases are more difficult to account for, such as the nonstatistical representativity of the selected set of individual radiation widths. In practice, an upper energy threshold exists above which only the neutron width can be extracted from the time-of-flight data. As this energy threshold depends on the neutron properties of the isotope under investigation and of the experimental conditions, it is often chosen arbitrarily. In the present work, this higher energy is determined by the relative uncertainty of the $\Gamma_{\lambda,\gamma}$ values, which must remain lower than $\pm 10\%$.

The Bayes threshold for $l$ assignment, the upper energy limit of the statistical analysis and the energy threshold for determining the average radiation width are parameters that are fine tuned in order to achieve an overall consistency between the model parameters. In practice, such a consistency is reached via an iterative process based on the sequential analysis of the resonance and "continuum" ranges of the neutron cross sections.

Principles of the analysis of the resonance and "continuum" energy ranges are presented in Secs. III and IV, respectively.

## III. ANALYSIS OF THE RESOLVED RESONANCE RANGE

The resonance parameters (resonance energies $E_\lambda$, neutron widths $\Gamma_{\lambda,n}$, and radiation widths $\Gamma_{\lambda,\gamma}$) for neutron channels $c = \{l, J\}$ were determined with the resonance shape analysis code REFIT [24] using the Reich-Moore approximation [25] of the $R$-matrix theory [13]. In the present analysis, parameters were extracted up to 5 keV from transmission data measured at the GELINA facility of JRC-Geel in the late 1990s [12]. New sets of transmission data, also measured at the GELINA facility, were included in the analysis to specifically investigate the neutron energy range below 500 eV.

### A. Transmission data

The GELINA facility is based on an electron accelerator providing a pulsed white neutron source. For all the experiments used in this work, the accelerator was operated with a frequency of 800 Hz. At the exit of the accelerator, a compression magnet provides electron burst with a width less than 2 ns. Neutrons are produced by Bremsstrahlung radiations via the electrons slowdown in a water-moderated uranium target. Neutrons emitted from the target-moderator assembly are directed to the measurement stations through evacuated aluminum pipes. In the case of the transmission experiments investigated in this work, neutrons were detected by a Li-glass

TABLE I. List of transmission data measured at the GELINA facility with sample characteristics, filter set-up and energy range of interest for the resonance analysis. The three IRMM samples were used in Refs. [11,12], the JRC sample comes from JRC-Geel, and the TC99C sample comes from CEA of Cadarache. For the IRMM samples, measurements were performed at a $L = 49.33$ m station of GELINA. Those associated to JRC and TC99C samples were performed at $L = 10.861(2)$ m.

| Data Id | Sample geometry | Sample thickness | Sample diameter | Powder form | Areal or volume number density | Antioverlap and black resonance filters | Energy Range in eV |
|---|---|---|---|---|---|---|---|
| $IRMM_1$ | cylindrical | 5 mm | 50 mm | $^{99}Tc_4\,Al_{11}$+Sulfur | $9.72(39) \times 10^{-4}$ at/b | – | [3−200] |
| $IRMM_2$ | cylindrical | 5 mm | 50 mm | $^{99}Tc_4\,Al_{11}$+Sulfur | $2.65(11) \times 10^{-3}$ at/b | – | [3−500] |
| $IRMM_3$ | cylindrical | 5 mm | 50 mm | $^{99}Tc$ | $2.49(10) \times 10^{-2}$ at/b | – | [3−5000] |
| $JRC_1$ | cylindrical | 8 mm | 13 mm | $^{99}TcO_2$ | $6.41(26) \times 10^{-3}$ at/b | B,Co,Na | [3−500] |
| $JRC_2$ | cylindrical | 8 mm | 13 mm | $^{99}TcO_2$ | $6.41(26) \times 10^{-3}$ at/b | B,Rh,Co,Na | [3−500] |
| $JRC_3$ | cylindrical | 8 mm | 13 mm | $^{99}TcO_2$ | $6.41(26) \times 10^{-3}$ at/b | Cd,Co,Na | [3−100] |
| $JRC_4$ | cylindrical | 8 mm | 13 mm | $^{99}TcO_2$ | $6.41(26) \times 10^{-3}$ at/b | Cd,Rh,Co,Na | [3−100] |
| $TC99C_1$ | rod | 95 mm | 8.1 mm | $^{99}Tc$+$^{nat}UO_2$ | $2.65(11) \times 10^{-3}$ at/b.cm | B,Co,Na | [3−650] |
| $TC99C_2$ | rod | 95 mm | 8.1 mm | $^{99}Tc$+$^{nat}UO_2$ | $2.65(11) \times 10^{-3}$ at/b.cm | Cd,Co,Na | [3−100] |
| $TC99C_3$ | rod (shifted) | 95 mm | 8.1 mm | $^{99}Tc$+$^{nat}UO_2$ | $2.65(11) \times 10^{-3}$ at/b.cm | B,Co,Na | [3−650] |
| $TC99C_4$ | rod (shifted) | 95 mm | 8.1 mm | $^{99}Tc$+$^{nat}UO_2$ | $2.65(11) \times 10^{-3}$ at/b.cm | Cd,Co,Na | [3−100] |

detector. Neutron spectroscopy experiments carried out at the GELINA facility are based on the time-of-flight technique that consists in connecting the neutron energies $E$ to their flight time $t$, given the flight path length $L$ between the neutron source and the detectors.

A neutron transmission measurement consists in measuring the neutron flux attenuation through a sample whose size can be smaller or larger than the neutron beam diameter. The quantity of interest $T_{exp}$, can be obtained from the counting spectra $C$ after subtracting the background $B$ as follows:

$$T_{exp}(t) = N_T \frac{[C_{in}(t) - B_{in}(t)] - \alpha[C_{out}(t) - B_{out}(t)]}{(1-\alpha)[C_{out}(t) - B_{out}(t)]}, \quad (10)$$

in which indexes indicate the sample positions (sample "in" or "out" of the beam) and $\alpha$ represents the void fraction. Its value depends on the sample geometry and beam diameter. The void fraction is $\alpha = 0$ for samples larger than the neutron beam. Otherwise, $\alpha$ can be estimated from black resonances of the nuclides contained in the sample. The time-of-flight spectra are corrected for dead-time. They are normalized to the TOF bin and to the integrated count rate of $BF_3$ counters, located in the ceiling of the neutron target hall. The normalization factor $N_T = 1.0$ is then introduced in the Eq. (10) to account for a global uncertainty of $\pm 0.5\%$, which is mainly due to variations in the beam intensity and electronics. The time-dependent background was determined via the black-resonance technique. Parameters of simple analytical functions are adjusted at the bottom of known black resonances originating from filters placed in the neutron beam.

The list of transmission data included in the analysis is reported in Table I together with a few experimental characteristics. Three types of data can be distinguished depending on which sample is involved. These samples were not specifically prepared for the present work. They already existed and were reused for our measurements. The first data set (IRMM) corresponds to transmission data whose analysis is described in Refs. [11,12]. The three samples had a cylindrical shape with diameters larger than the neutron beam (void fraction $\alpha = 0$). The transmission measurements were performed at an $L = 49.33$ m station of GELINA in the late 1990s. The second data set (JRC) encompasses four transmission data measured with the same cylindrical sample having a diameter larger than the neutron beam (void fraction $\alpha = 0$). It was designed for past experiments at the Van de Graaff facility of JRC-Geel. Unfortunately, the number of $^{99}$Tc atoms contained in the JRC sample was not well known. The value of $6.41(26) \times 10^{-3}$ at/b reported in Table I were then determined together with the resonance parameters. Transmission spectra of the third data set (TC99C) were measured with a cylindrical rod containing ten $UO_2$ pellets doped with $^{99}$Tc. This sample was specifically designed for pile-oscillation measurements in the MINERVE reactor at the CEA Cadarache Research Centre [26]. In that case, the beam diameter is larger than the diameter of the rod (8.1 mm). The void fraction $\alpha$ was determined thanks to well known $^{238}$U resonances observed in the transmission data. For this sample, measurements were performed with the rod well aligned to the neutron beam and slightly shifted from the central position in order to investigate the impact of the neutron beam profile on the final results. The full data reduction procedures handled with the AGS code are described in Refs. [27,28].

Time-of-flight data measured at the GELINA facility are shown in Fig. 2. For the JRC and TC99C samples, the different sequences of black-resonance and antioverlap filters provide equivalent transmission data. Main discrepancies occur at the position of the Cd resonance energies. Otherwise, no meaningful differences can be observed, even if the TC99C sample is slightly shifted from the central position (Fig. 3). Geometrical characteristics of these samples make them of great interest to verify and complement results provided by the thickest IRMM sample ($IRMM_3$), especially for the first $^{99}$Tc resonance at 5.6 eV. Moreover, in the transmission data measured with the TC99C sample, the closeness of the $^{238}$U and $^{99}$Tc resonances ensures an internal cross-check of the various data reduction steps. The newly measured transmission data also aims at providing additional information on the total width of the low energy resonances for a better estimation of the radiation widths.

### B. Theoretical transmission

The transmission data listed in Table I were all included in a simultaneous analysis using the REFIT code. The latter code is able to account for cylindrical rods with a radius $r$ lower than the beam radius $R$ containing $k$ nuclides having a volume number density $\rho_k$. The generic expression of the theoretical transmission can be written as follows [27,28]:

$$T_{th}(E) = \frac{\int_{-r}^{r} \sqrt{1-(x/R)^2}\exp\left[-2r\sqrt{1-(x/r)^2}\left(\sum_k \rho_k \sigma_{\mathrm{tot}_k}(E)\right)\right]dx}{\int_{-r}^{r}\sqrt{1-(x/R)^2}dx}. \tag{11}$$

This transmission depends on the Doppler broadened total cross section $\sigma_{\mathrm{tot}_k}$ of each nuclide $k$. A free gas model is routinely used to calculate $\sigma_{\mathrm{tot}_k}$ at an effective temperature $T_{\mathrm{eff}}$.

For a cylindrical sample with $r > R$ and a thickness $h = 2r$, the square root $\sqrt{1-(x/r)^2}$ becomes equal to unity and Eq. (11) reduces to the simple form:

$$T_{th}(E) = \exp\left[-h\left(\sum_k \rho_k \sigma_{\mathrm{tot}_k}(E)\right)\right]. \tag{12}$$

Neutron resonances observed in the time-of-flight data can only be compared with their theoretical analogues after a correct broadening of the theoretical transmission:

$$T(t) = \int R(t,E)T_{th}(E)\mathrm{d}E, \tag{13}$$

in which the probability density functions $R(t,E)$ stand for the time-dependent experimental response function of the spectrometer. The main contribution to $R(t,E)$ is the neutron transport in the target-moderator assembly of the GELINA facility. Parameters of analytical expressions implemented in the REFIT code were optimized using Monte Carlo simulations and $^{238}$U resonances observed in the transmission data.

Figure 4 shows some resonances observed up to 200 eV with the posterior theoretical curves provided by REFIT. The $^{99}$Tc resonance parameters are free parameters, while those of $^{238}$U come from the evaluated neutron library JEFF-3.3. A good overall agreement is achieved between all the data sets measured with the IRMM, JRC, and TC99C samples (Table I). Local discrepancies remain within the experimental uncertainties, even in the case of strong overlap between $^{99}$Tc and $^{238}$U resonances for the TC99C sample. Around 124 eV, only data measured with the three IRMM samples are used because of the presence of noisy structures in the other transmission spectra due to the Co filter (Fig. 2).

The $^{99}$Tc resonance parameters, reported in the Appendix, have been obtained following an iterative analysis between the resonance and "continuum" energy ranges. Therefore, the principles of the optical model calculations are presented in Sec. IV and final model parameters are discussed in Sec. V.

## IV. ANALYSIS OF THE "CONTINUUM" ENERGY RANGE

Neutron cross sections above the resonance range are treated as average cross sections. Total, shape-elastic scattering, and reaction cross sections are described in the framework of the $S$-matrix theory by using phenomenological optical model potentials. The reaction cross section is split into partial neutron reactions by using a statistical model. In the present work, both mechanisms are handled with the TALYS code [29] that provides an easy-to-use interface for the optical model code ECIS [30]. In the present work, we limit ourselves in the optimization of the optical model parameters to the experimental total cross sections of $^{99}$Tc.

### A. Total neutron cross section data

In the keV neutron energy range, no reliable total average cross section was reported in the literature. A single accurate data set was reported by Foster and Glasgow [31] in the neutron energy range between 2.5 MeV to 15 MeV. $^{99}$Tc results were reported together with 92 other data sets covering a wide mass range from hydrogen to plutonium. This systematic work allowed the authors to reduce the systematic uncertainties down to 2%.

We have complemented the data of Foster and Glasgow with the transmission data measured with the thick IRMM sample, labeled IRMM$_3$ in Table I. The transmission data were converted in total cross section, averaged over a broad energy mesh and corrected for resonance self-shielding for spanning the neutron energies from 150 eV to 150 keV. A similar treatment was applied in Ref. [12], but only within 10 keV to 150 keV. The combination of the low and high energy data sets will provide valuable information for establishing optical model parameters over a wider energy range.

### B. Theoretical total cross section

The theoretical total cross section was calculated using the ECIS code via a suitable interface provided by TALYS. In the present work, we assumed that $^{99}$Tc is weakly deformed. We found that the optical model of Morillon *et al.* [32,33] was suitable for reproducing the data up to several tens of MeV. The dispersive optical potential can be written as

$$\begin{aligned} V(r,E) = {} & [(V_v(E)+\Delta V_v(E)) + iW_v(E)]f(r,r_0,a) \\ & - 4a[\Delta V_s(E) + iW_s(E)]\frac{df(r,r_0,a)}{dr} \\ & - [(V_{so}(E)+\Delta V_{so}(E)) + iW_{so}(E)]\left(\frac{h}{m_\pi c}\right)^2 \\ & \times \frac{1}{r}\frac{df(r,r_0,a)}{dr}\overrightarrow{l}\,\overrightarrow{s}, \end{aligned} \tag{14}$$

where the Woods-Saxon form factors $f(r,r_0,a)$ for the volume ($v$), surface ($s$), and spin-orbit ($so$) potentials share the same geometrical parameters (nuclear radius $R$ and diffuseness $a$):

$$R = (r_0 - 2.7\times 10^{-4}A)A^{1/3}\ (\text{in fm}), \tag{15}$$

$$a = a_0 + 5\times 10^{-9}A^3\ (\text{in fm}). \tag{16}$$

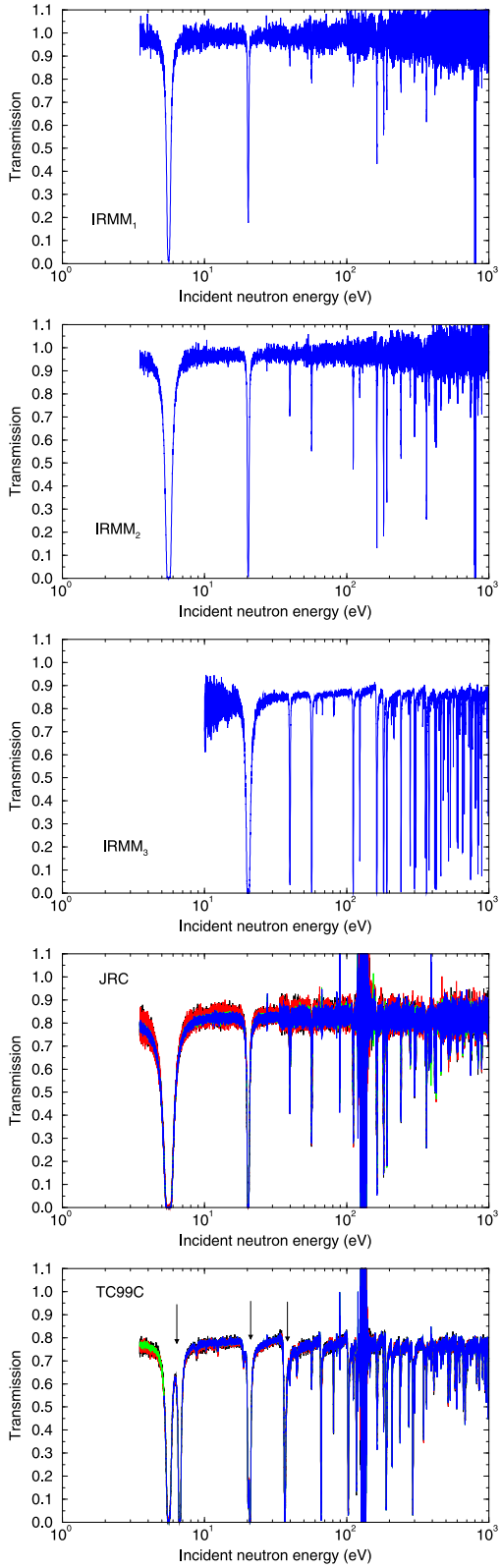


FIG. 2. $^{99}$Tc transmission data measured at the GELINA facility up to 1 keV with the IRMM, JRC, and TC99C samples. Sample characteristics and filter set-up are given in Table I. Noisy structures observed around 132 eV are due to black resonance of Co. Arrows in the bottom plot locate the three first $^{238}$U resonances at 6.7 eV, 20.9 eV and 36.7 eV.

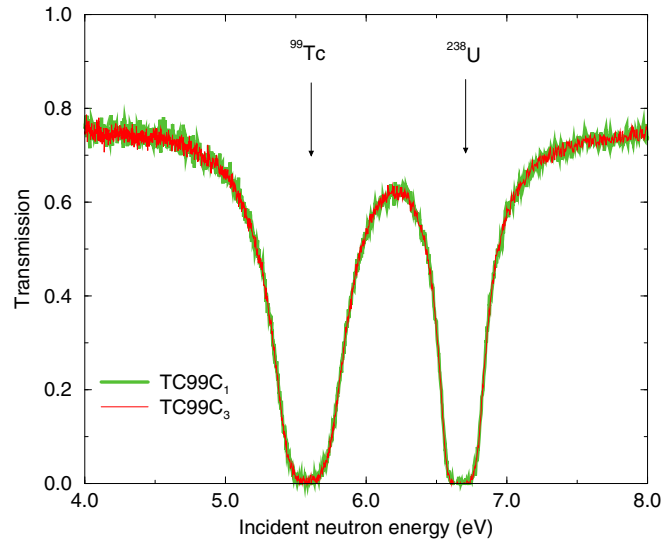


FIG. 3. Comparison of transmission measurements performed with the TC99C sample well aligned to the neutron beam (TC99C$_1$) and slightly shifted from the central position (TC99C$_3$).

In the dispersion relation treatment, $\Delta V_i(E)$ is used to connect the real $V_i(E)$ and imaginary $W_i(E)$ terms of each component $(i = v, s, so)$. For the spin-orbit contributions, $V_{so}(E)$ and $W_{so}(E)$ were taken from Ref. [34]. For the real part of the surface potential the Hartree-Fock contribution of the mean field is given by

$$V_v(E) = V_{HF}\ e^{(-\frac{\mu\beta^2[E-E_F]}{2\hbar^2})} e^{(\frac{4\mu^2\gamma^2[E-E_F]^2}{\hbar^4})}. \quad (17)$$

This contribution is defined by the depth $V_{HF}$, the reduced mass of the system $\mu$, and the nonlocality ranges $\beta$ and $\gamma$. For the volume and surface imaginary terms, the energy dependencies are symmetric about the Fermi energy $E_F$:

$$W_v(E) = \frac{A_v(E-E_F)^2}{(E-E_F)^2 + B_v^2}, \quad (18)$$

$$W_s(E) = \frac{A_s(E-E_F)^2}{(E-E_F)^2 + B_s^2}\exp(-C_s(E-E_F)). \quad (19)$$

Parameters of interest for this work are the reduced radius $r_0$, the diffuseness $a_0$, and the depths $V_{HF}$, $A_v$, and $A_s$.

The least-squares minimization procedure implemented in the CONRAD code [35] was used to optimize the optical model parameters on the experimental cross sections, briefly introduced in Sec. IV A. Posterior values are reported in Table II. The quoted uncertainties and correlations account for the normalization uncertainties (close to 4%) of the experimental total cross sections. Large uncertainties are obtained for $A_v$ and $A_s$. The strong correlation of 0.96 between these two parameters reflects the lack of experimental data which is required to constrain their values. Figure 5 compares the experimental and theoretical total cross sections, calculated up to 100 MeV with the parameters listed in Table II. The calculated relative uncertainty lies between $\pm 4\%$ to $\pm 26\%$. Results obtained in the low energy range are given in Table III.

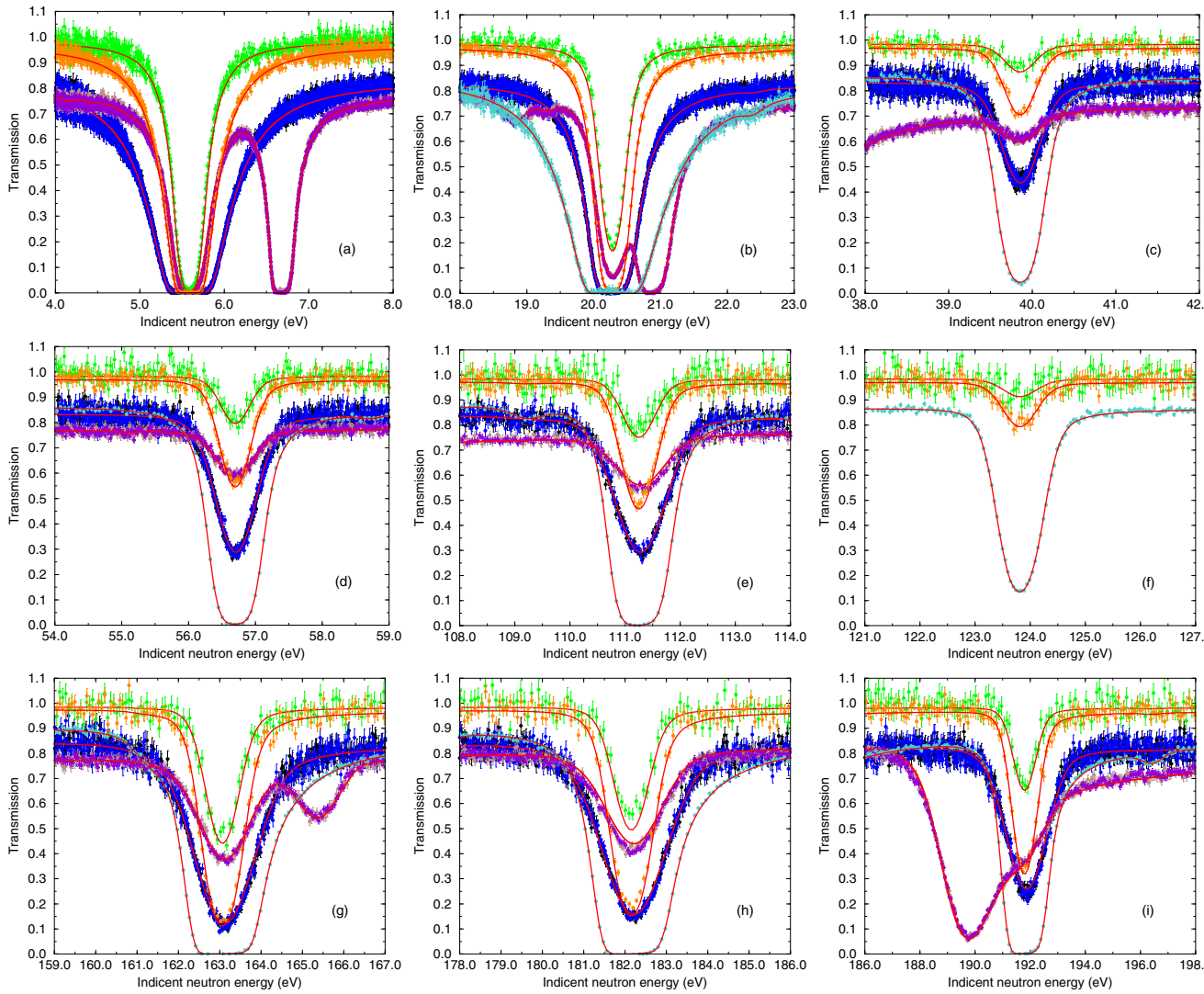


FIG. 4. Examples of REFIT calculations (red solid line) compared to transmission data measured at the GELINA facility with the IRMM, JRC, and TC99C samples (Table I). For the JRC and TC99C samples, only data measured with the boron antioverlap filter are displayed.

Above 3 keV, the differences between the experimental values and the theory remain within the quoted uncertainties.

Similarly to the resonance range, the optical model calculations presented in this section are the results of an iterative analysis between the resonance and "continuum" energy ranges. This approach aims at providing consistent $l$-dependent neutron strength function $S_l$ and channel radius $a_c$, which are discussed in the next section.

TABLE II. Optical model parameters, uncertainties and correlation matrix obtained in this work for the nuclear system $^{99}$Tc $+n$.

| Parameters | | Values | Rel. Unc. | Correlation matrix | | | | |
|---|---|---|---|---|---|---|---|---|
| $r_0$ | (fm) | 1.35(3) | 2.2% | 100 | | | | |
| $a_0$ | (fm) | 0.53(2) | 3.8% | 9 | 100 | | | |
| $V_{HF}$ | (MeV) | −72.8(19) | 2.6% | 57 | 87 | 100 | | |
| $A_v$ | (MeV) | 21.7(33) | 15.2% | −56 | 75 | 36 | 100 | |
| $A_s$ | (MeV) | 22.0(23) | 10.5% | −75 | −72 | −96 | −11 | 100 |

## V. DISCUSSIONS

The resonance analysis (Sec. III) followed by the analysis of the "continuum" energy range (Sec. IV) provides prior model parameters that have to be optimized until reaching consistent average resonance parameters between the low and high energy model calculations. In practice, calculations are repeated iteratively by updating a few parameters which are the Bayes threshold for $l$ assignment, the upper energy limit of the statistical analysis and the energy threshold for determining the average radiation width.

### A. Average radiation width

The energy threshold above which an average radiation width is used in the resonance analysis can be chosen according to the relative uncertainty obtained on the individual $\Gamma_{\lambda,\gamma}$ values. Figure 6 shows that above 200 eV the relative uncertainties become higher than 10% and the spread between the values increases with the incident neutron energy. Calcu-

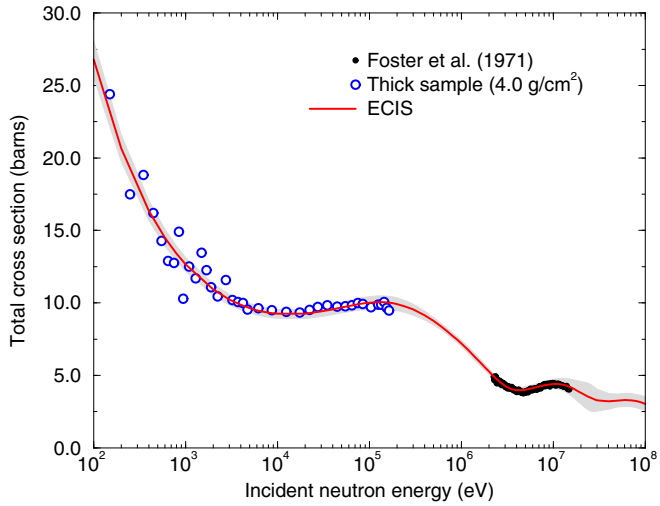


FIG. 5. $^{99}$Tc total cross section calculated with the ECIS module of the TALYS code, compared to data reported by Foster and Glasgow [31] and those deduced from the transmission measured with the thick IRMM sample [12]. The shadow area represents the uncertainty band due to systematic uncertainties.

lations become more sensitive to the area of the resonances, which is closely related to the neutron width. By considering nine resonances below 200 eV, the Monte Carlo propagation of the resonance parameter uncertainties and correlations leads to

$$\langle \Gamma_{\gamma_0} \rangle = 137(7) \text{ meV } (5.1\%).$$

This result represents the two first moments of the distribution shown in Fig. 7. Our work confirms the value recommended by Mughaghab [137(8) meV] [36] which is slightly lower than the weighted mean value of 147(10) meV obtained from the past analysis of the GELINA data. In the present analysis, no attempt was made to estimate an average radiation width for *p*-wave resonances. We assumed that $\langle \Gamma_{\gamma_0} \rangle = \langle \Gamma_{\gamma_1} \rangle$.

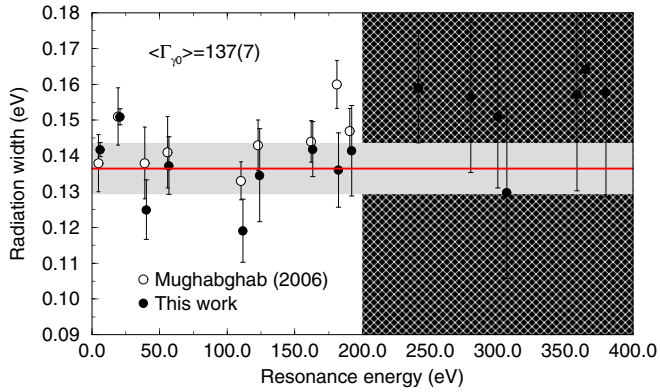


FIG. 6. *s*-wave radiation widths obtained in this work and compared to those compiled by Mughaghab [36]. Only values below 200 eV are used to calculate the average radiation width.

TABLE III. $^{99}$Tc total cross sections as a function of the incident neutron energy deduced from the transmission data measured with the thick IRMM sample and calculated with the ECIS module of the TALYS code. The quoted uncertainties account for the normalization uncertainty (close to 4%).

| Energy (eV) | Experimental value (barns) | Theoretical result (barns) | Rel. unc. (%) |
|---|---|---|---|
| 150 | 24.41 | 23.02(102) | 4.4 |
| 250 | 17.50 | 19.17(82) | 4.3 |
| 350 | 18.84 | 17.11(71) | 4.1 |
| 450 | 16.21 | 15.80(64) | 4.1 |
| 550 | 14.29 | 14.88(60) | 4.0 |
| 650 | 12.91 | 14.18(56) | 4.0 |
| 750 | 12.76 | 13.64(53) | 3.9 |
| 850 | 14.92 | 13.20(51) | 3.9 |
| 950 | 10.30 | 12.83(48) | 3.8 |
| 1100 | 12.53 | 12.47(46) | 3.7 |
| 1300 | 11.70 | 12.12(45) | 3.7 |
| 1500 | 13.46 | 11.83(43) | 3.6 |
| 1700 | 12.27 | 11.58(42) | 3.6 |
| 1900 | 11.10 | 11.36(41) | 3.6 |
| 2250 | 10.45 | 11.04(39) | 3.5 |
| 2750 | 11.58 | 10.67(37) | 3.5 |
| 3250 | 10.21 | 10.37(36) | 3.5 |
| 3750 | 10.08 | 10.12(35) | 3.4 |
| 4250 | 9.99 | 9.91(34) | 3.4 |
| 4750 | 9.54 | 9.72(33) | 3.4 |
| 6250 | 9.64 | 9.51(32) | 3.4 |
| 8750 | 9.50 | 9.32(31) | 3.4 |
| 12500 | 9.39 | 9.30(32) | 3.4 |
| 17500 | 9.34 | 9.39(34) | 3.6 |
| 22500 | 9.52 | 9.46(35) | 3.7 |
| 27500 | 9.74 | 9.51(36) | 3.7 |
| 35000 | 9.84 | 9.58(36) | 3.8 |
| 45000 | 9.77 | 9.65(38) | 3.9 |
| 55000 | 9.79 | 9.72(39) | 4.0 |
| 65000 | 9.86 | 9.80(40) | 4.1 |
| 75000 | 10.01 | 9.86(42) | 4.2 |
| 85000 | 9.94 | 9.92(43) | 4.3 |
| 105000 | 9.72 | 10.00(44) | 4.4 |
| 125000 | 9.90 | 9.97(44) | 4.5 |
| 135000 | 9.90 | 9.96(45) | 4.5 |
| 145000 | 10.07 | 9.95(45) | 4.5 |
| 155000 | 9.67 | 9.94(45) | 4.5 |
| 165000 | 9.49 | 9.93(45) | 4.5 |

### B. Neutron strength function and mean level spacing

Results from any statistical analysis of the resonance parameters mainly depend on two parameters. The first parameter is the Bayes threshold for $l$ assignment. The second parameter is the upper energy limit of the statistical analysis. In the present work, these two parameters are part of the same code, namely ESTIMA [37]. It allows us to fine tune these two parameters in order to obtain a consistent description of the *s*-wave cumulative distribution function of the Porter-Thomas law, of the cumulative distribution of the *s*-wave reduced neutron widths and of the cumulative distribution of

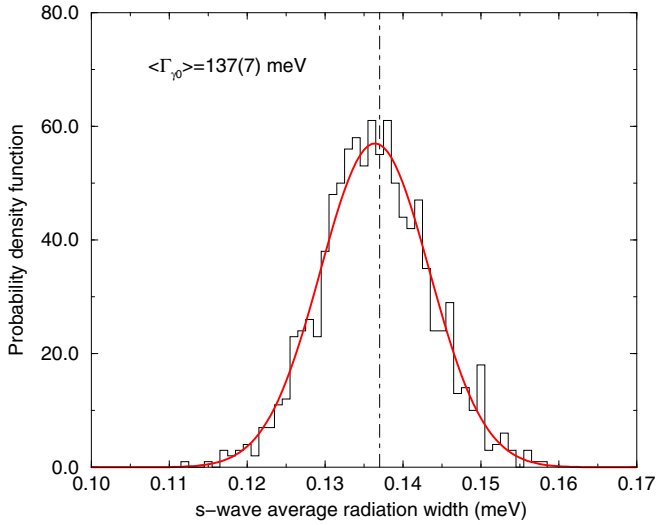


FIG. 7. Distribution of the s-wave average radiation width obtained from the Monte Carlo propagation of the resonance parameter uncertainties and correlations. The two first moments of the distribution provides the $\langle\Gamma_{\gamma_0}\rangle$ value and its uncertainty.

the number of $s$-wave resonances. This approach provides a simultaneous estimation of the $s$-wave neutron strength function $S_0$ and mean level spacing $D_0$ by taking into account missing resonances. Few trial and error tests lead to the conclusion that an upper energy limit $E_{\max} = 3$ keV fulfilled the conditions of having a fraction of missing levels lower than 5%. According to this choice, the Bayes threshold for $l$ assignment was found to be close to 0.5, meaning that a given resonance having a Bayesian conditional probability greater than 0.5 is likely to be a $p$-wave resonance. Results of the ESTIMA analysis are summarized in Fig. 8. The least-squares fit of the cumulative distribution function of the reduced neutron widths leads to the following values:

$$S_0 = 0.51(6) \times 10^{-4},$$
$$D_0 = 12.8(2)\ \text{eV},$$

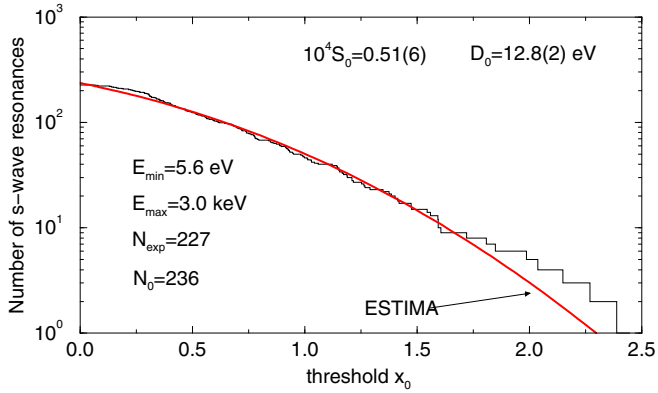


FIG. 8. Cumulative distribution function of the reduced neutron widths calculated between $E_{\min} = 5.6$ eV and $E_{\max} = 3$ keV.

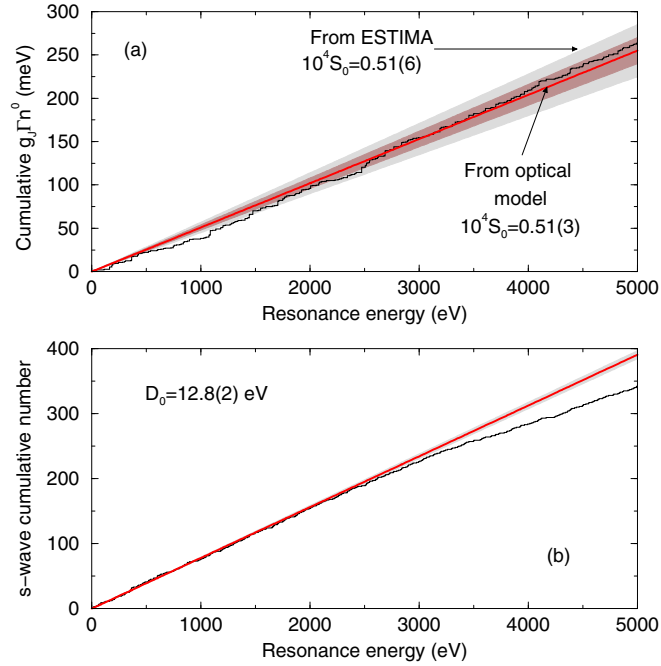


FIG. 9. Staircase plots of the $s$-wave reduced neutron widths (a) and of the cumulative number of $s$-wave resonances (b). The slope of the distributions provides the neutron strength function $S_0$ and the level density $1/D_0$, respectively. The shadow areas represent the uncertainty band.

which are in excellent agreement with the staircase plots shown in Fig. 9, suggesting that 64 resonances of small amplitude are missing below 5 keV. The neutron strength function can also be calculated with Eq. (6). The optical model parameters of Table II lead to

$$S_0 = 0.51(3) \times 10^{-4}.$$

The iterative analysis between the resonance and "continuum" energy ranges succeeded in converging to the same neutron strength function with a reduction by a factor two of the uncertainty on $S_0$. By contrast, Eq. (6) provides $p$- and $d$-wave neutron strength functions

$$S_1 = 5.7(19) \times 10^{-4},$$
$$S_2 = 0.91(14) \times 10^{-4},$$

with large relative uncertainties of about 33% and 15%, respectively. The correlation coefficient between these two parameters is $-0.73$. We face an indeterminate parameters problem due to the lack of experimental constraints between these two parameters. The present result is consistent with the lack of constraints already pointed out between the optical model parameters $A_v$ and $A_s$ (Table II). Despite such uncertainties, the compensation between the $p$- and $d$-wave contributions provides total cross section uncertainties that remain lower than 5% over a wide neutron energy range. The consequence on the theoretical capture cross section in the keV energy range is discussed in Sec. V D.

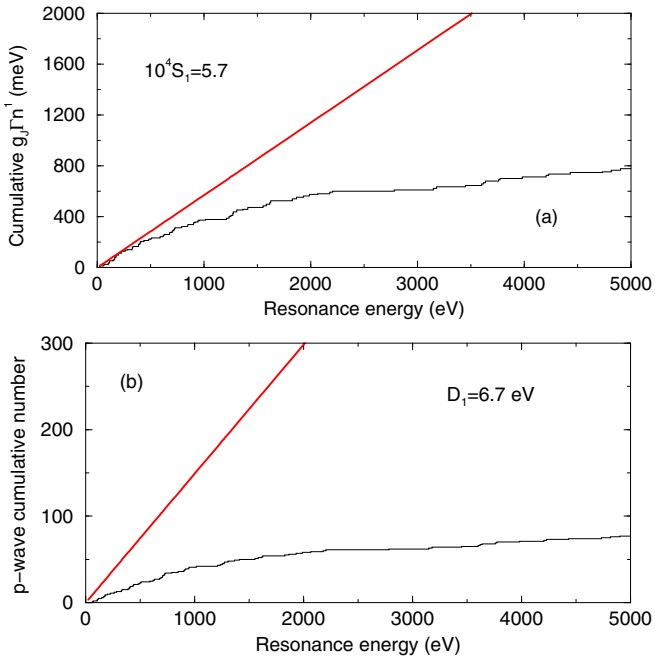


FIG. 10. Staircase plots of the $p$-wave reduced neutron widths (a) and of the cumulative number of $p$-wave resonances (b). The slope of the distributions should provide the neutron strength function $S_1$ and the level density $1/D_1$, respectively.

The staircase plot of the $p$-wave reduced neutron widths [Fig. 10(a)] confirms the lack of reliable information on $S_1$ due to the small fraction of $p$-wave resonances identified in the resonance range [Fig. 10(b)], assuming that the order of magnitude of $D_1 = 6.7$ eV is correctly predicted by the level density composite formula of Gilbert and Cameron [38].

The present study confirms the recommendations of Mughaghab which are $S_0 = 0.49(6) \times 10^{-4}$, $S_1 = 5.8(8) \times 10^{-4}$, $D_0 = 12.8(5)$ eV, and $D_1 = 6.8(3)$ eV [36].

### C. Channel and effective radius

The channel radius $a_c$ is used in the $R$-matrix formalism to calculate the phase-shift $\phi_l^{SQW}$ [Eq. (5)] and the centrifugal-barrier penetration factor $P_l^{SQW}$ [Eq. (7)]. Its value can be estimated via the phase-shift $\phi_l^{OMC}$ originating from the complex mean-field potential that was optimized for $^{99}$Tc. Figure 11 shows the ECIS results calculated with the optical model parameters reported in Table II. The equivalent $l$-dependent phase shifts in the square-well approximation are obtained with the following channel radii:

$$a_0 = 6.52(9)\ \text{fm},$$
$$a_1 = 7.6(12)\ \text{fm},$$
$$a_2 = 5.85(14)\ \text{fm}.$$

The energy-dependent behavior of $\phi_0^{OMC}$ and $\phi_2^{OMC}$ is adequately reproduced with the square-well approximation up to several hundreds of keV. The large uncertainty ($\pm 16\%$) quoted for the $p$-wave radius $a_1$ reflects the shape difference observed between $\phi_1^{OMC}$ and $\phi_1^{SQW}$ in Fig. 11. This unsolved

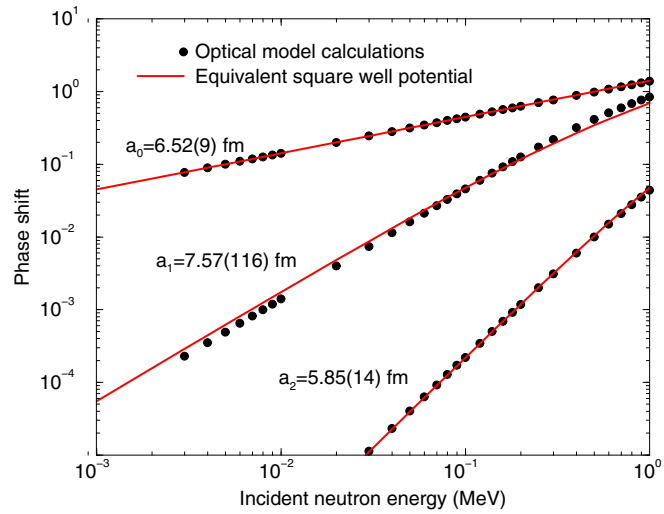


FIG. 11. $l$-dependent phase shift calculated with the optical model parameters of Table II and with the square-well approximation [Eq. (5)].

issue would require additional studies for determining the origin of the differences specifically observed for $l = 1$.

For channel $c$ having zero orbital momentum, the channel radius $a_0$ is equivalent to the potential scattering length or effective radius $R'$. Most of the empirical expressions suggest choosing $R'$ greater than the nuclear radius by an amount roughly equal to the diffuseness [39]. For $^{99}$Tc, the combination of Eqs. (15) and (16) with parameters $r_0 = 1.35$ and $a_0 = 0.53$ reported in Table II, the expression of Foster and Glasgow ($R' = 1.28A^{1/3} + 0.53$) or the one prescribed in the Evaluated Nuclear Data Files ($R' = 1.23A^{1/3} + 0.8$) lead to effective radii respectively equal to 6.65 fm, 6.45 fm, and 6.49 fm, which are all in excellent agreement with our result [$R' = 6.52(9)$ fm].

### D. Capture cross section

The theoretical capture cross section is provided by the TALYS code, in which the $\gamma$-ray transmission coefficients are normalized to $T_{\gamma_0}$ [Eq. (3)] and the neutron transmission coefficients [Eq. (4)] are calculated with the optical model parameters of Table II. $T_{\gamma_0}$ depends on the average radiation width [$\langle\Gamma_{\gamma_0}\rangle = 137(7)$ meV] and mean level spacing [$D_0 = 12.8(2)$ eV] whose values are discussed in Secs. V A and V B.

Figure 12 shows the TALYS results calculated between 1 keV and 1 MeV. The dashed lines correspond to the partial wave contributions for $l = 0, 1, 2$. At $E = 30$ keV, we obtain a capture cross section of

$$\sigma_\gamma(30\ \text{keV}) = 1076(45)\ \text{mb}.$$

The present result is dominated by the $p$-wave contribution. As discussed in Sec. V B, the $p$-wave neutron strength function $S_1 = 5.7(19)$ deduced from the optical model calculations is characterized by a large relative uncertainty of about 33%, which may has an impact on the accuracy of the capture cross section in the keV energy range. A sensibility study of the capture cross section at $E = 30$ keV to the model

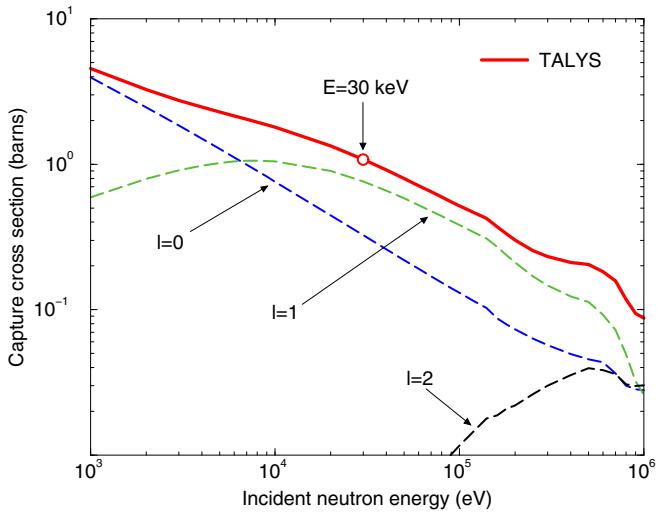


FIG. 12. $^{99}$Tc capture cross section calculated with the TALYS code. The dashed lines show the $s$-wave ($l = 0$), $p$-wave ($l = 1$), and $d$-wave ($l = 2$) contributions.

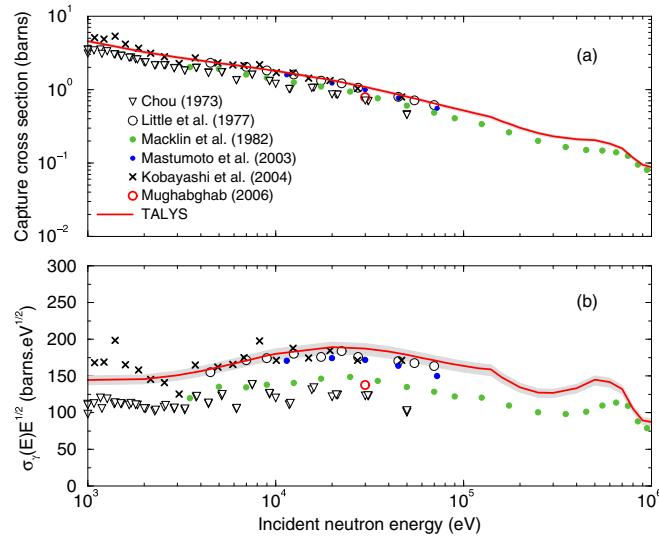


FIG. 13. The top plot (a) shows the $^{99}$Tc capture cross section (in barns) calculated with the TALYS code. It is compared with data reported in the experimental library EXFOR [40]. The red open circle locates the value at $E = 30$ keV compiled by Mughaghab in his Atlas of Neutron Resonances [36]. The bottom plot (b) shows the same capture cross section times the square root of the incident neutron energy. The shadow area represents the uncertainty band due to the model parameter uncertainties.

parameters indicates that the uncertainties due to the average radiation width, optical model parameters and $s$-wave mean level spacing are equal to ±35, ±27, ±7 mb, respectively. Despite the non-negligible contribution of the optical model parameters, the average radiation width uncertainty dominates the final capture cross section uncertainty.

The theoretical values of the $^{99}$Tc capture cross section are reported in Table IV up to 1.2 MeV. The relative uncertainty increases slowly with the incident neutron energy from ±4.1% to ±6.4%. It remains close to the relative uncertainty of the average radiation width (±5.1%) because the neutron energy dependence uncertainty of the $\gamma$-ray transmission coefficients is not taken into account in the present work. The latter mainly depends on the giant dipole resonance and level density formalisms. A specific study would be needed to address the impact of these missing sources of uncertainties with the increasing incident neutron energy.

TABLE IV. $^{99}$Tc capture cross sections as a function of the incident neutron energy calculated with the TALYS code. The quoted uncertainties account for the propagation of the uncertainties of the optical model parameters (Table II), average radiation width (5.1%), and mean level spacing (1.6%).

| Energy (keV) | $(n,\gamma)$ (mb) | Rel. unc. (%) | Energy (keV) | $(n,\gamma)$ (mb) | Rel. unc. (%) |
|---|---|---|---|---|---|
| 1 | 4556(185) | 4.1 | 80 | 591(27) | 4.5 |
| 2 | 3247(134) | 4.1 | 90 | 549(25) | 4.5 |
| 3 | 2746(115) | 4.2 | 100 | 514(23) | 4.5 |
| 4 | 2470(104) | 4.2 | 120 | 461(21) | 4.6 |
| 5 | 2285(97) | 4.2 | 140 | 422(19) | 4.6 |
| 6 | 2148(91) | 4.2 | 160 | 368(17) | 4.7 |
| 7 | 2038(86) | 4.2 | 180 | 330(16) | 4.7 |
| 8 | 1945(82) | 4.2 | 200 | 299(14) | 4.7 |
| 9 | 1865(78) | 4.2 | 250 | 253(11) | 4.5 |
| 10 | 1794(75) | 4.2 | 300 | 230(10) | 4.4 |
| 20 | 1332(55) | 4.1 | 400 | 210(9) | 4.3 |
| 30 | 1076(45) | 4.2 | 500 | 204(9) | 4.3 |
| 40 | 911(39) | 4.3 | 600 | 182(8) | 4.4 |
| 50 | 795(35) | 4.3 | 700 | 157(7) | 4.4 |
| 60 | 709(31) | 4.4 | 800 | 117(5) | 4.6 |
| 70 | 643(29) | 4.5 | 900 | 94(5) | 5.1 |
| 80 | 591(27) | 4.5 | 1000 | 87(5) | 5.7 |
| 90 | 549(25) | 4.5 | 1200 | 70(5) | 6.4 |

The TALYS results is compared with data reported in the literature in Fig. 13. The bottom plot highlights the large differences between the experimental data. Two groups of data sets can be distinguished, suggesting normalization issues. Our calculations confirm the higher experimental values reported by Little [41], Matsumoto [42], and Kobayashi [43]. At $E = 30$ keV, we obtain a capture cross section which is significantly higher than the value recommended by Mughaghab [795(40) mb]. Our result is in excellent agreement with the capture cross section of Little interpolated at 30 keV [1044(89) mb]. It remains within the limit of the quoted uncertainties in the case of Matsumoto's data [994(43) mb]. The agreement with those of Kobayashi (≈1020 mb) is not relevant because large uncertainties (±25%) are reported by the Japanese team.

The corresponding Maxwellian-averaged cross section (MACS) at $kT = 30$ keV deduced from our calculations is

$$\langle \sigma_\gamma(30\ \text{keV}) \rangle = 1016(43)\ \text{mb}.$$

This result supports the value of 933(47) mb compiled in the Karlsruhe Astrophysical Database of Nucleosynthesis in Stars (KADoNiS) [44]. This recommended value comes from capture cross section measurements performed at the GELINA

facility [45]. Such an agreement confirms that similar average capture cross sections and uncertainties can be obtained in the keV energy range from transmission measurements with an iterative analysis between the resonance and "continuum" energy ranges as proposed in the present work.

## VI. CONCLUSIONS

The total neutron cross section of $^{99}$Tc was evaluated up to 100 MeV thanks to transmission measurements performed at the GELINA facility from 3 eV to 150 keV and the total cross section measured by Foster and Glasgow between 2.5 MeV and 15 MeV. An iterative analysis between the resonance and "continuum" energy ranges allowed us to establish a set of model parameters in good agreement with those reported in the literature. Energies $E_\lambda$, radiation widths $\Gamma_{\lambda,\gamma}$, and neutron widths $\Gamma_{\lambda,n}$ of the resonances $\lambda$ were extracted with the REFIT code up to 5 keV. Optical model parameters involved in the ECIS module of the TALYS code were optimized to obtain a set of average resonance parameters [$S_0 = 0.51(3)$, $\langle\Gamma_{\gamma_0}\rangle = 137(7)$ meV, $D_0 = 12.8(2)$ eV] fully consistent between the low and high energy nuclear models. Such an agreement was achieved by fine-tuning a few threshold parameters, namely the Bayes threshold for $l$ assignment (meaning that a resonance is likely a $p$ wave for a Bayesian conditional probability greater than 0.5), the upper energy limit of the statistical analysis of the resonance parameters (<3 keV) and the energy threshold for determining the average radiation width (<200 eV).

The $^{99}$Tc average capture cross section was calculated with the TALYS code by using the average parameters established in this work. A value of 1076(45) mb was obtained at 30 keV. The rather low relative uncertainty of $\pm 4.1\%$ is mainly dominated by the average radiation width uncertainty ($\pm 5.1\%$). Further studies are needed to account for the neutron energy dependence uncertainty of the $\gamma$-ray transmission coefficients.

Our theoretical approach provides a Maxwellian-averaged cross section at $kT = 30$ keV equal to 1016(43) mb, in reasonable agreement with the value of 933(47) mb compiled in the KADoNiS database, which has been directly established from capture measurements. Such an agreement confirms that reliable capture cross sections in the keV energy range can be achieved from transmission data by using the iterative analysis proposed in this work. It yields valuable perspectives for the modeling of neutron-induced capture-reaction on long-lived fission products.

## ACKNOWLEDGMENTS

The authors wish to express their appreciations for the experimental work performed at the JRC-Geel (Belgium) with the support of the EUFRAT project.

## APPENDIX: $^{99}$Tc RESONANCE PARAMETERS OBTAINED IN THIS WORK UP TO 5 keV

Table V reports the resonance parameters established in this work up to 1 keV. The experimental data used in the analysis are described in Sec. III. Principles of the $l$ assignment

TABLE V. $^{99}$Tc resonance parameters below 1 keV obtained from the simultaneous analysis of the transmission data listed in Table I. The average radiation width is set to $\langle\Gamma_{\gamma_0}\rangle = 137(7)$ meV. We assumed that $\langle\Gamma_{\gamma_0}\rangle = \langle\Gamma_{\gamma_1}\rangle$.

| $E_\lambda$ (eV) | Unc. (eV) | $J^\pi$ ($\hbar$) | $\Gamma_{\lambda,\gamma}$ (meV) | Unc. (meV) | $\Gamma_{\lambda,n}$ (meV) | Unc. (meV) |
|---|---|---|---|---|---|---|
| 5.59 | 0.01 | $5^+$ | 141.8 | 2.0 | 3.70 | 0.12 |
| 14.60 | 0.01 | $3^-$ | 137.0 | 7.0 | ≈0.01 | |
| 20.28 | 0.01 | $4^+$ | 150.9 | 2.2 | 8.70 | 0.34 |
| 22.39 | 0.01 | $5^-$ | 137.0 | 7.0 | ≈0.01 | |
| 39.86 | 0.02 | $5^+$ | 125.0 | 8.4 | 1.07 | 0.06 |
| 56.70 | 0.03 | $4^+$ | 137.3 | 8.1 | 3.94 | 0.20 |
| 58.75 | 0.03 | $6^-$ | 137.0 | 7.0 | ≈0.01 | |
| 61.46 | 0.04 | $3^-$ | 137.0 | 7.0 | 0.09 | 0.01 |
| 66.11 | 0.04 | $5^-$ | 137.0 | 7.0 | ≈0.01 | |
| 67.69 | 0.04 | $4^-$ | 137.0 | 7.0 | 0.09 | 0.01 |
| 81.00 | 0.05 | $3^-$ | 137.0 | 7.0 | 0.16 | 0.01 |
| 81.77 | 0.05 | $6^-$ | 137.0 | 7.0 | 0.08 | 0.01 |
| 102.89 | 0.06 | $4^-$ | 137.0 | 7.0 | 0.04 | 0.01 |
| 109.24 | 0.06 | $3^-$ | 137.0 | 7.0 | 0.11 | 0.01 |
| 111.27 | 0.06 | $5^+$ | 119.1 | 8.8 | 10.45 | 0.51 |
| 114.24 | 0.07 | $5^-$ | 137.0 | 7.0 | 0.05 | 0.01 |
| 123.84 | 0.08 | $4^+$ | 134.6 | 13.0 | 4.10 | 0.22 |
| 148.38 | 0.09 | $3^-$ | 137.0 | 7.0 | 0.12 | 0.02 |
| 161.30 | 0.09 | $5^-$ | 137.0 | 7.0 | 0.19 | 0.02 |
| 163.07 | 0.09 | $5^+$ | 141.9 | 7.7 | 58.92 | 3.04 |
| 173.21 | 0.10 | $4^-$ | 137.0 | 7.0 | 0.15 | 0.02 |
| 177.54 | 0.10 | $6^-$ | 137.0 | 7.0 | 0.07 | 0.01 |
| 182.16 | 0.10 | $4^+$ | 136.1 | 10.4 | 72.93 | 3.49 |
| 191.80 | 0.11 | $5^+$ | 141.4 | 12.7 | 37.13 | 2.16 |
| 196.45 | 0.11 | $3^-$ | 137.0 | 7.0 | 0.29 | 0.03 |
| 206.49 | 0.17 | $4^+$ | 137.0 | 7.0 | 0.69 | 0.09 |
| 210.05 | 0.16 | $4^-$ | 137.0 | 7.0 | 0.49 | 0.08 |
| 214.92 | 0.18 | $4^+$ | 137.0 | 7.0 | 1.19 | 0.11 |
| 220.73 | 0.19 | $5^-$ | 137.0 | 7.0 | 0.49 | 0.07 |
| 226.09 | 0.03 | $4^-$ | 137.0 | 7.0 | 0.28 | 0.03 |
| 241.26 | 0.13 | $4^+$ | 137.0 | 7.0 | 38.63 | 2.21 |
| 261.72 | 0.15 | $3^-$ | 137.0 | 7.0 | 0.32 | 0.05 |
| 273.23 | 0.16 | $3^-$ | 137.0 | 7.0 | 1.02 | 0.06 |
| 280.04 | 0.16 | $4^+$ | 137.0 | 7.0 | 15.30 | 0.77 |
| 282.44 | 0.16 | $6^-$ | 137.0 | 7.0 | 0.06 | 0.03 |
| 300.14 | 0.29 | $4^+$ | 137.0 | 7.0 | 38.08 | 3.79 |
| 305.15 | 0.18 | $5^-$ | 137.0 | 7.0 | 0.54 | 0.04 |
| 306.97 | 0.30 | $5^+$ | 137.0 | 7.0 | 14.72 | 0.78 |
| 317.80 | 0.04 | $6^-$ | 137.0 | 7.0 | 0.54 | 0.02 |
| 324.73 | 0.04 | $5^-$ | 137.0 | 7.0 | 0.47 | 0.05 |
| 333.29 | 0.04 | $6^-$ | 137.0 | 7.0 | 0.25 | 0.04 |
| 343.40 | 0.36 | $5^+$ | 137.0 | 7.0 | 1.65 | 0.15 |
| 350.26 | 0.04 | $3^-$ | 137.0 | 7.0 | 1.39 | 0.09 |
| 356.19 | 0.21 | $5^-$ | 137.0 | 7.0 | 0.65 | 0.05 |
| 358.85 | 0.37 | $4^+$ | 137.0 | 7.0 | 20.20 | 1.04 |
| 361.55 | 0.21 | $5^-$ | 137.0 | 7.0 | 1.06 | 0.07 |
| 362.78 | 0.21 | $4^+$ | 137.0 | 7.0 | 1.97 | 0.16 |
| 365.14 | 0.36 | $5^+$ | 137.0 | 7.0 | 146.96 | 8.53 |
| 380.08 | 0.42 | $5^+$ | 137.0 | 7.0 | 21.65 | 1.25 |
| 386.25 | 0.22 | $5^-$ | 137.0 | 7.0 | 0.62 | 0.06 |
| 398.42 | 0.23 | $3^-$ | 137.0 | 7.0 | 0.60 | 0.10 |
| 403.12 | 0.23 | $3^-$ | 137.0 | 7.0 | 0.53 | 0.10 |
| 410.55 | 0.24 | $4^-$ | 137.0 | 7.0 | 0.13 | 0.07 |

TABLE V. *(Continued).*

| $E_\lambda$ (eV) | Unc. (eV) | $J^\pi$ ($\hbar$) | $\Gamma_{\lambda,\gamma}$ (meV) | Unc. (meV) | $\Gamma_{\lambda,n}$ (meV) | Unc. (meV) |
|---|---|---|---|---|---|---|
| 413.05 | 0.24 | $5^-$ | 137.0 | 7.0 | 0.97 | 0.07 |
| 416.93 | 0.24 | $4^+$ | 137.0 | 7.0 | 66.15 | 3.61 |
| 426.66 | 0.25 | $5^+$ | 137.0 | 7.0 | 62.42 | 3.45 |
| 433.38 | 0.25 | $6^-$ | 137.0 | 7.0 | 0.11 | 0.06 |
| 439.91 | 0.25 | $3^-$ | 137.0 | 7.0 | 0.43 | 0.12 |
| 447.82 | 0.27 | $5^+$ | 137.0 | 7.0 | 2.24 | 0.21 |
| 460.18 | 0.26 | $4^+$ | 137.0 | 7.0 | 43.13 | 2.43 |
| 465.78 | 0.27 | $6^-$ | 137.0 | 7.0 | 0.85 | 0.08 |
| 479.06 | 0.27 | $4^+$ | 137.0 | 7.0 | 12.99 | 0.76 |
| 480.99 | 0.28 | $4^-$ | 137.0 | 7.0 | 0.63 | 0.10 |
| 486.86 | 0.28 | $5^+$ | 137.0 | 7.0 | 5.43 | 0.38 |
| 496.81 | 0.29 | $6^-$ | 137.0 | 7.0 | 0.09 | 0.06 |
| 506.97 | 0.29 | $6^-$ | 137.0 | 7.0 | 0.38 | 0.08 |
| 515.45 | 0.50 | $4^+$ | 137.0 | 7.0 | 13.34 | 0.81 |
| 519.56 | 0.50 | $5^+$ | 137.0 | 7.0 | 30.13 | 1.69 |
| 526.68 | 0.30 | $4^-$ | 137.0 | 7.0 | 1.76 | 0.12 |
| 535.56 | 0.53 | $4^+$ | 137.0 | 7.0 | 30.97 | 1.69 |
| 563.65 | 0.74 | $5^+$ | 137.0 | 7.0 | 8.10 | 0.56 |
| 566.97 | 0.07 | $6^-$ | 137.0 | 7.0 | 1.05 | 0.15 |
| 589.07 | 0.34 | $6^-$ | 137.0 | 7.0 | 0.51 | 0.10 |
| 594.00 | 0.32 | $4^+$ | 137.0 | 7.0 | 6.38 | 0.54 |
| 598.43 | 0.33 | $5^+$ | 137.0 | 7.0 | 26.99 | 1.58 |
| 599.84 | 0.33 | $5^+$ | 137.0 | 7.0 | 3.04 | 0.42 |
| 607.02 | 0.33 | $4^+$ | 137.0 | 7.0 | 38.56 | 2.15 |
| 617.61 | 0.36 | $3^-$ | 137.0 | 7.0 | 1.51 | 0.21 |
| 623.76 | 0.35 | $4^+$ | 137.0 | 7.0 | 5.59 | 0.51 |
| 630.81 | 0.36 | $5^-$ | 137.0 | 7.0 | 0.47 | 0.14 |
| 632.84 | 0.36 | $5^+$ | 137.0 | 7.0 | 2.45 | 0.32 |
| 655.24 | 0.93 | $4^+$ | 137.0 | 7.0 | 47.95 | 2.74 |
| 672.80 | 0.97 | $5^+$ | 137.0 | 7.0 | 21.97 | 1.33 |
| 675.75 | 0.08 | $4^-$ | 137.0 | 7.0 | 1.34 | 0.20 |
| 686.80 | 3.73 | $5^+$ | 137.0 | 7.0 | 5.27 | 0.68 |
| 690.29 | 0.08 | $3^-$ | 137.0 | 7.0 | 0.63 | 0.26 |

TABLE V. *(Continued).*

| $E_\lambda$ (eV) | Unc. (eV) | $J^\pi$ ($\hbar$) | $\Gamma_{\lambda,\gamma}$ (meV) | Unc. (meV) | $\Gamma_{\lambda,n}$ (meV) | Unc. (meV) |
|---|---|---|---|---|---|---|
| 699.66 | 0.08 | $6^-$ | 137.0 | 7.0 | 0.22 | 0.12 |
| 702.51 | 0.08 | $5^-$ | 137.0 | 7.0 | 0.88 | 0.17 |
| 716.95 | 0.09 | $6^-$ | 137.0 | 7.0 | 0.54 | 0.14 |
| 721.10 | 0.09 | $6^-$ | 137.0 | 7.0 | 0.77 | 0.14 |
| 724.43 | 0.09 | $5^+$ | 137.0 | 7.0 | 8.53 | 0.66 |
| 727.61 | 0.09 | $4^-$ | 137.0 | 7.0 | 0.47 | 0.21 |
| 745.72 | 0.09 | $4^+$ | 137.0 | 7.0 | 119.14 | 6.70 |
| 753.96 | 0.09 | $4^+$ | 137.0 | 7.0 | 64.71 | 3.55 |
| 766.46 | 0.09 | $4^+$ | 137.0 | 7.0 | 11.03 | 0.82 |
| 774.89 | 0.09 | $5^+$ | 137.0 | 7.0 | 2.93 | 0.29 |
| 791.01 | 0.10 | $4^-$ | 137.0 | 7.0 | 1.41 | 0.30 |
| 799.04 | 0.10 | $4^+$ | 137.0 | 7.0 | 5.08 | 0.31 |
| 805.99 | 0.10 | $5^+$ | 137.0 | 7.0 | 28.19 | 1.69 |
| 816.32 | 0.10 | $5^+$ | 137.0 | 7.0 | 25.28 | 1.54 |
| 828.46 | 0.10 | $4^+$ | 137.0 | 7.0 | 4.24 | 0.29 |
| 839.14 | 0.10 | $4^+$ | 137.0 | 7.0 | 123.48 | 7.08 |
| 845.30 | 0.10 | $5^-$ | 137.0 | 7.0 | 1.78 | 0.31 |
| 847.72 | 0.10 | $4^+$ | 137.0 | 7.0 | 62.29 | 3.51 |
| 851.58 | 0.10 | $6^-$ | 137.0 | 7.0 | 1.90 | 0.20 |
| 872.54 | 0.10 | $3^-$ | 137.0 | 7.0 | 4.23 | 0.89 |
| 874.01 | 0.11 | $4^+$ | 137.0 | 7.0 | 6.08 | 0.63 |
| 876.37 | 0.11 | $5^+$ | 137.0 | 7.0 | 13.31 | 1.07 |
| 893.19 | 0.11 | $4^+$ | 137.0 | 7.0 | 144.19 | 8.51 |
| 899.05 | 0.11 | $5^-$ | 137.0 | 7.0 | 1.43 | 0.30 |
| 904.59 | 0.11 | $5^-$ | 137.0 | 7.0 | 0.55 | 0.29 |
| 915.81 | 0.11 | $3^-$ | 137.0 | 7.0 | 1.22 | 0.41 |
| 927.50 | 0.11 | $4^+$ | 137.0 | 7.0 | 4.74 | 0.40 |
| 943.31 | 0.11 | $5^-$ | 137.0 | 7.0 | 1.42 | 0.30 |
| 950.59 | 0.11 | $5^-$ | 137.0 | 7.0 | 0.57 | 0.14 |
| 972.34 | 0.12 | $5^+$ | 137.0 | 7.0 | 11.01 | 0.97 |
| 981.73 | 0.12 | $4^-$ | 137.0 | 7.0 | 4.20 | 0.20 |
| 995.22 | 0.12 | $4^+$ | 137.0 | 7.0 | 53.51 | 3.20 |
| 1008.50 | 0.12 | $4^-$ | 137.0 | 7.0 | 3.88 | 0.50 |

are presented in Sec. V B, given that no attempt was made to establish the spin of the resonances. They are taken from the evaluated neutron cross section library JEFF-3.3 [8]. The origin of the average radiation width is discussed in Sec. V A. The quoted uncertainties were obtained from a Monte Carlo propagation of the experimental uncertainties. The technique is not discussed in the present work. More details can be found elsewhere [46].


[1] P. W. Merrill, Astrophys. J. **116**, 21 (1952).
[2] T. Lebzelter and J. Hron, Astron. Astrophys. **411**, 533 (2003).
[3] S. Uttenthaler *et al.*, Astron. Astrophys. **463**, 251 (2007).
[4] D. Rochman *et al.*, Nucl. Sci. Eng. **158**, 68 (2008).
[5] N. Iwamoto, J. Nucl. Sci. Techno. **49**, 244 (2012).
[6] N. Iwamoto and T. Katabuchi, EPJ Web Conf. **146**, 02049 (2017).
[7] T. Katabuchi *et al.*, EPJ Web Conf. **146**, 11050 (2017).
[8] A. Plompen *et al.*, Eur. Phys. J. A **56**, 181 (2020).
[9] D. A. Brown *et al.*, Nucl. Data Sheets **148**, 1 (2018).
[10] K. Shibata *et al.*, J. Nucl. Sci. Technol. **48**, 1 (2011).
[11] C. Brienne-Raepsaet, Nouvelle determination des parametres de resonances neutronique de $^{99}$Tc, Ph.D. thesis, Aix-Marseille Universiy, 1998.
[12] F. Gunsing, A. Lepretre, C. Mounier, C. Raepsaet, A. Brusegan, and E. Macavero, Phys. Rev. C **61**, 054608 (2000).
[13] A. M. Lane and R. G. Thomas, Rev. Mod. Phys. **30**, 257 (1958).
[14] W. H. Dickhoff and R. J. Charity, Prog. Part. Nucl. Phys. **105**, 252 (2019).
[15] H. Feshbach, C. E. Porter, and V. F. Weisskopf, Phys. Rev. **96**, 448 (1954).
[16] G. Noguere, Contribution to the study of the unresolved resonance range of the neutron cross sections, CEA Report No. CEA-R-6398, 2015.
[17] Y. Xu, S. Goriely, A. J. Koning, and S. Hilaire, Phys. Rev. C **90**, 024604 (2014).
[18] D. Rochman *et al.*, Phys. Lett. B **764**, 109 (2017).

[19] W. Hauser and H. Feshbach, Phys. Rev. **87**, 366 (1952).
[20] P. A. Moldauer, Phys. Rev. C **11**, 426 (1978).
[21] E. Rich *et al.*, Nucl. Sci. Eng. **162**, 76 (2009).
[22] C. De Saint Jean *et al.*, Nucl. Sci. Eng. **161**, 363 (2009).
[23] C. E. Porter and R. G. Thomas, Phys. Rev. **104**, 483 (1956).
[24] M. C. Moxon and J. B. Brisland, REFIT computer code, Harwell Laboratory Report No. CBNM/ST/90-131/1, 1990.
[25] C. W. Reich and M. S. Moore, Phys. Rev. **111**, 929 (1958).
[26] A. Gruel *et al.*, Nucl. Sci. Eng. **169**, 229 (2011).
[27] L. Salamon, Transmission and capture cross section measurements by the time-of-flight technique for validation of pile-oscillation experiments in the Minerve reactor, Ph.D. thesis, Aix-Marseille University, 2011.
[28] L. Salamon *et al.*, J. Radioanal. Nucl. Chem. **321**, 519 (2019).
[29] A. J. Koning *et al.*, in *Proceedings of the International Conference on Nuclear Data for Science and Technology, Santa Fe, New Mexico, 2004*, edited by R. C. Haight *et al.* (American Institute of Physics, New York, 2005).
[30] J. Raynal, in *Proceedings of the Specialists' Meeting on the Nucleon Nucleus Optical Model up to 200 MeV, Bruyeres-le-Chatel, Ance, 1996* (Nuclear Energy Agency, Paris, 1997).
[31] D. G. Foster and D. W. Glasgow, Phys. Rev. C **3**, 576 (1971).
[32] B. Morillon and P. Romain, Phys. Rev. C **70**, 014601 (2004).
[33] B. Morillon and P. Romain, Phys. Rev. C **74**, 014601 (2006).
[34] A. J. Koning and J. P. Delaroche, Nucl. Phys. A **713**, 231 (2003).
[35] P. Archier *et al.*, Nucl. Data Sheets **118**, 488 (2014).
[36] S. F. Mughabghab, *Atlas of Neutron Resonances*, 5th ed. (Elsevier, Amsterdam, 2006).
[37] E. Fort andJ. P. Doat, ESTIMA computer code, NEA Nuclear Data Committee Report No. NEANDC-161U, 1983.
[38] A. Gilbert and A. G. W. Cameron, Can. J. Phys. **43**, 1446 (1965).
[39] E. Vogt, R-Matrix theory, R-Matrix School of the Joint Institute for Nuclear Astrophysics, Notre Dame University, Indiana, USA, 2004, https://www.semanticscholar.org/paper/R-matrix-Theory∗-Vogt/0480fbc3c273182d3be03843b4e51e350c0e0106.
[40] H. Henriksson *et al.*, in *Proceedings of the International Conference on Nuclear Data for Science and Technology, Nice, France, 2007*, edited by O. Bersillon *et al.* (EDP Science, Paris, 2008).
[41] R. C. Little and R. C. Block, Trans. Am. Nucl. Soc. **26**, 574 (1977).
[42] T. Matsumoto *et al.*, J. Nucl. Sci. Technol. **40**, 61 (2003).
[43] K. Kobayashi *et al.*, Nucl. Sci. Eng. **146**, 209 (2004).
[44] I. Dillmann *et al.*, AIP Conf. Proc. **819**, 123 (2006).
[45] F. Gunsing *et al.*, Nucl. Phys. A **688**, 496 (2001).
[46] G. Noguere *et al.*, Nucl. Sci. Eng. **160**, 108 (2008).